



HAL
open science

Superconfined falling liquid films: linear versus nonlinear dynamics

Gianluca Lavallo, Sophie Mergui, Nicolas Grenier, Georg F. Dietze

► **To cite this version:**

Gianluca Lavallo, Sophie Mergui, Nicolas Grenier, Georg F. Dietze. Superconfined falling liquid films: linear versus nonlinear dynamics. *Journal of Fluid Mechanics*, 2021, 919 (R2), 10.1017/jfm.2021.417 . hal-03236774

HAL Id: hal-03236774

<https://hal.science/hal-03236774>

Submitted on 18 Aug 2021

HAL is a multi-disciplinary open access archive for the deposit and dissemination of scientific research documents, whether they are published or not. The documents may come from teaching and research institutions in France or abroad, or from public or private research centers.

L'archive ouverte pluridisciplinaire **HAL**, est destinée au dépôt et à la diffusion de documents scientifiques de niveau recherche, publiés ou non, émanant des établissements d'enseignement et de recherche français ou étrangers, des laboratoires publics ou privés.

Superconfined falling liquid films: linear versus nonlinear dynamics

Journal:	<i>Journal of Fluid Mechanics</i>
Manuscript ID	JFM-21-RP-0089.R2
mss type:	JFM Rapids
Date Submitted by the Author:	30-Apr-2021
Complete List of Authors:	Lavalle, Gianluca; UMR5307 Grenier, Nicolas; Laboratoire d'Informatique pour la Mecanique et les Sciences de l'Ingenieur Mergui, Sophie; Fluides Automatique et Systemes Thermiques Dietze, Georg; CNRS, Laboratoire FAST - UMR 7608
JFM Keywords:	Thin films < Interfacial Flows (free surface), Instability, Gas/liquid flows < Multiphase and Particle-laden Flows
Abstract:	<p>The effect of a counter-current gas flow on the linear stability of an inclined falling liquid film switches from destabilizing to stabilizing, as the flow confinement is increased. We confront this linear effect with the response of nonlinear surface waves resulting from long-wave interfacial instability. For the strongest confinement studied, the gas flow damps both the linear growth rate and the amplitude of nonlinear travelling waves, and this holds for waves of the most-amplified frequency and for low-frequency solitary waves. In the latter case, waves are shaped into elongated humps with a flat top that resist secondary instabilities. For intermediate confinement, the linear and nonlinear responses are opposed and can be non-monotonic. The linear growth rate of the most-amplified waves first decreases and then increases as the gas velocity is increased, whereas their nonlinear amplitude is first amplified and then damped. Conversely, solitary waves are amplified linearly but damped nonlinearly. For the weakest confinement, solitary waves are prone to two secondary instability modes that are not observed in unconfined falling films. The first involves waves of diminishing amplitude slipstreaming toward their growing leading neighbours. The second causes wave splitting events that lead to a train of smaller, shorter waves.</p>

SCHOLARONE™
Manuscripts

Banner appropriate to article type will appear here in typeset article

1 Superconfined falling liquid films: linear versus 2 nonlinear dynamics

3 Gianluca Lavallo¹, Sophie Mergui^{2,4}, Nicolas Grenier³, and Georg F. Dietze^{2†}

4 ¹Mines Saint-Etienne, Univ Lyon, CNRS, UMR 5307 LGF, Centre SPIN, F-42023 Saint-Etienne, France.

5 ²Université Paris-Saclay, CNRS, FAST, 91405, Orsay, France.

6 ³Université Paris-Saclay, CNRS, LISN, 91405, Orsay, France.

7 ⁴Sorbonne Université, Faculté des Sciences et Ingénierie, UFR d'Ingénierie, F-75005 Paris, France.

8 (Received xx; revised xx; accepted xx)

9 The effect of a counter-current gas flow on the linear stability of an inclined falling liquid film
10 switches from destabilizing to stabilizing, as the flow confinement is increased. We confront
11 this linear effect with the response of nonlinear surface waves resulting from long-wave
12 interfacial instability. For the strongest confinement studied, the gas flow damps both the
13 linear growth rate and the amplitude of nonlinear travelling waves, and this holds for waves
14 of the most-amplified frequency and for low-frequency solitary waves. In the latter case,
15 waves are shaped into elongated humps with a flat top that resist secondary instabilities.
16 For intermediate confinement, the linear and nonlinear responses are opposed and can be
17 non-monotonic. The linear growth rate of the most-amplified waves first decreases and then
18 increases as the gas velocity is increased, whereas their nonlinear amplitude is first amplified
19 and then damped. Conversely, solitary waves are amplified linearly but damped nonlinearly.
20 For the weakest confinement, solitary waves are prone to two secondary instability modes
21 that are not observed in unconfined falling films. The first involves waves of diminishing
22 amplitude slipstreaming toward their growing leading neighbours. The second causes wave
23 splitting events that lead to a train of smaller, shorter waves.

24 **Key words:** Thin films

25 1. Introduction

26 We consider a gravity-driven two-dimensional liquid film falling down a plane tilted at an
27 angle ϕ w.r.t. the horizontal, in contact with a counter-current gas flow that is strongly
28 confined by an upper wall placed at $y=H$ (figure 1). Both fluids are Newtonian with
29 constant fluid properties and the flow is laminar. Confined falling liquid films occur in
30 rectification columns for cryogenic air separation, which contain structured packings that
31 subdivide the column cross-section into millimetric channels (Valluri *et al.* 2005). Even
32 stronger confinement is realized in compact reflux condensers (Vlachos *et al.* 2001), falling

† Email address for correspondence: dietze@fast.u-psud.fr

2

G. Lavalle, S. Mergui, N. Grenier, and G. F. Dietze

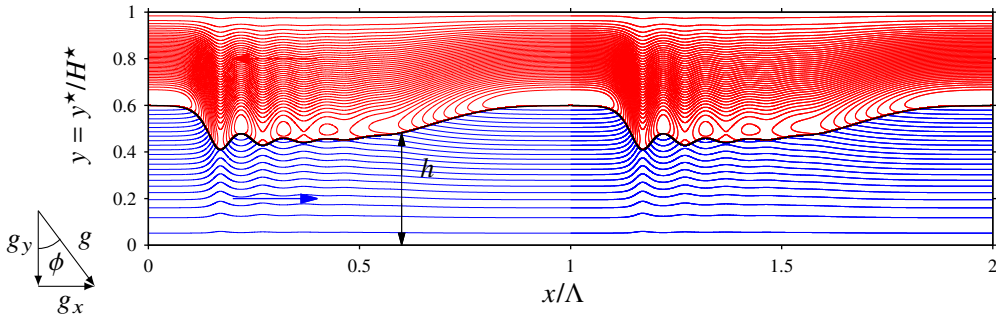


Figure 1: Problem sketch: gravity-driven falling liquid film (lower blue streamlines) in contact with a counter-current gas flow (upper red streamlines) flowing through a channel of dimensional gap height H^* inclined at an angle ϕ w.r.t. the horizontal. Streamlines (separated by constant stream function increments) are shown in the wall-fixed reference frame, and Λ is the wavelength.

33 film microreactors (Zhang *et al.* 2009), and micro-gap coolers (Kabov *et al.* 2011). We are
 34 interested in nonlinear waves that form on the surface of the falling liquid film due to the
 35 long-wave Kapitza instability (Kapitza 1948), and, in particular, how these are affected by the
 36 gas velocity in a strongly-confined setting. Such waves are known to trigger flooding events,
 37 either by local obstruction of the channel, flow reversal, or wave reversal (Vlachos *et al.*
 38 2001; Trifonov 2010a; Tseluiko & Kalliadasis 2011).

39 For weak confinements, flooding seems to be favoured by decreasing the gap height and/or
 40 increasing the gas flow rate. Experiments (Kofman *et al.* 2017) and numerical simulations
 41 (Trifonov 2010a,b) alike have shown that the amplitude of nonlinear waves increases with
 42 increasing counter-current gas flow and that this growth diverges in the vicinity of the
 43 flooding point (Drosos *et al.* 2006). Moreover, actual flooding experiments have shown
 44 that the critical gas flow rate decreases with diminishing gap height (Sudo 1996). Linear
 45 stability investigations, which demonstrate an increase in the maximal linear growth rate
 46 with increasing gas velocity, tend to confirm this nonlinear picture (Alekseenko *et al.* 2009;
 47 Vellingiri *et al.* 2015; Schmidt *et al.* 2016; Trifonov 2017).

48 On the other hand, recent investigations suggest that strong confinements may, in fact,
 49 lower the risk of flooding. Lavalle *et al.* (2019) have shown that the Kapitza instability can
 50 be entirely suppressed by sufficiently confining the gas, as suggested by Tilley *et al.* (1994)
 51 and confirmed by Kushnir *et al.* (2021), and that this is facilitated by low tilt angles. Further,
 52 the authors observed that the linear stabilization, which they confirmed experimentally, is
 53 amplified by increasing the counter-current gas flow rate. Recent nonlinear direct numerical
 54 simulations (DNS) of inclined falling liquid films (Trifonov 2020) have identified a non-
 55 monotonic variation of the interfacial velocity, mean film thickness, and inter-phase friction
 56 coefficient with increasing counter-current gas velocity, although the trend of the wave
 57 amplitude remained monotonic and increasing.

58 These investigations have motivated us to take a closer look at strongly-confined *inclined*
 59 falling liquid films, in contrast to Dietze & Ruyer-Quil (2013) and Lavalle *et al.* (2020), who
 60 studied the vertical configuration, where the gas-induced linear stabilization is relatively
 61 weak. This is because the inertia-induced destabilizing mechanism of the Kapitza instability
 62 is weakened less and less by the stabilizing effect of normal gravity as the tilt angle is
 63 increased, and thus the relative weight of the gas effect diminishes (Lavalle *et al.* 2019).
 64 We aim to confront linear stability predictions with the response of nonlinear surface waves
 65 to an increasingly strong counter-current gas flow. In particular, we wish to know whether
 66 nonlinear travelling waves can be damped under the effect of the gas flow, in line with the

67 linear observations, and, if so, whether they may resist secondary instability. Such a situation
 68 would amount to a reduced flooding risk. By *secondary instability* we mean the loss of
 69 stability of travelling-wave solutions (TWS) produced by the primary Kapitza instability
 70 (Liu & Gollub 1993; Lavalle *et al.* 2020), and our analysis is restricted to two-dimensional
 71 such instability modes.

72 An enticing preliminary result was obtained by Samanta (2014), who showed that applying
 73 a constant interfacial shear stress to an inclined wavy falling liquid film can strongly reduce
 74 the amplitude of nonlinear surface waves. However, for the strong confinement studied here,
 75 variations of the shear stress with wave height play an important role (Lavalley *et al.* 2019),
 76 and the gas pressure gradient, which was also neglected in the model of Samanta (2014),
 77 needs to be accounted for (Dietze & Ruyer-Quil 2013).

78 To tackle this problem, we use the two-phase weighted residual integral boundary layer
 79 (WRIBL) model of Dietze & Ruyer-Quil (2013) to construct TWS, with the continuation
 80 software Auto07P (Doedel 2008), and to compute spatially evolving wavy falling liquid films,
 81 with our own finite-difference code (Lavalley *et al.* 2020). These nonlinear computations are
 82 confronted with linear stability calculations based on the WRIBL model, and solutions of
 83 the full Orr-Sommerfeld (OS) eigenvalue problem (Tilley *et al.* 1994), whereby we have
 84 employed a spatial stability formulation (Barmak *et al.* 2016). Also, we check for periodic
 85 secondary instabilities via transient periodic computations started from TWS (Lavalley *et al.*
 86 2020), and confront our model with a direct numerical simulation (DNS) based on the full
 87 Navier-Stokes equations, using the finite-volume solver `Basilisk` (Popinet 2015).

88 Our manuscript is structured as follows. The mathematical description and numerical
 89 methods are introduced in §2, followed by section 3, which reports results of our linear and
 90 nonlinear computations. Subsection 3.1 is dedicated to surface waves of the linearly most-
 91 amplified frequency, whereas subsection 3.2 concerns low-frequency solitary waves (here,
 92 we will also introduce our DNS data). Conclusions are drawn in section 4.

93 2. Mathematical description

94 The flow in figure 1 is governed by the Navier-Stokes and continuity equations, written in
 95 Einstein notation using the directional indices $i=1,2$ and $j=1,2$ ($x_1=x$, $u_1=u$, $x_2=y$, and $u_2=v$),
 96 and the phase indicator m , which identifies liquid ($m=l$) and gas ($m=g$):

$$97 \quad X_m \partial_t u_i + u_j \partial_{x_j} u_i = -\partial_{x_i} p_m + \text{Re}_m^{-1} \partial_{x_j x_j} u_i + X_m^2 \text{Fr}^{-2} \{ \delta_{i1} \sin(\phi) - \delta_{i2} \cos(\phi) \}, \quad (2.1a)$$

$$98 \quad \partial_{x_j} u_j = 0, \quad (2.1b)$$

99 where lengths have been scaled with the channel height $\mathcal{L}=H^*$ (stars denote dimension-
 100 al quantities throughout), velocities with the phase-specific signed superficial velocities
 101 $\mathcal{U}_m=q_{m0}^*/H^*$, time with $\mathcal{T}=\mathcal{L}/\mathcal{U}_l$, and the phase-specific pressure p_m with $\rho_m \mathcal{U}_m^2$. Further,
 102 δ_{ij} is the Kronecker symbol, $X_l=1$, and $X_g=\mathcal{U}_l/\mathcal{U}_g$. The gravitational acceleration g enters
 103 through the Froude number $\text{Fr}=\mathcal{U}_l/\sqrt{g\mathcal{L}}$, and the Reynolds numbers $\text{Re}_m=\mathcal{U}_m \mathcal{L} \frac{\rho_m}{\mu_m}=q_{m0}^* \frac{\rho_m}{\mu_m}$
 104 are based on the phase-specific signed nominal flow rates q_{m0}^* of the flat-film primary flow,
 105 q_{g0}^* and Re_g being negative for a counter-current gas flow. The boundary conditions are:

$$106 \quad u_l|_{y=0} = v_l|_{y=0} = u_g|_{y=1} = v_g|_{y=1} = 0, \quad (2.1c)$$

107 and the kinematic and dynamic coupling conditions at the film surface $y=h(x, t)$:

$$108 \quad u_l = X_g^{-1} u_g, \quad v_l = X_g^{-1} v_g = \partial_t h + u_l \partial_x h, \quad (2.1d)$$

4

G. Lavalley, S. Mergui, N. Grenier, and G. F. Dietze

109

$$p_l + \left[S_{ij}^l n_j \right] n_i = X_g^{-2} \Pi_\rho p_g + X_g^{-1} \Pi_\mu \left[S_{ij}^g n_j \right] n_i + \text{We} \kappa, \quad (2.1e)$$

$$\left[S_{ij}^l n_j \right] \tau_i = X_g^{-1} \Pi_\mu \left[S_{ij}^g n_j \right] \tau_i, \quad (2.1f)$$

112 where $S_{ij}^m = \frac{1}{2} (\partial_{x_j} u_i + \partial_{x_i} u_j)$ denotes the strain rate tensor, $\Pi_\mu = \mu_g / \mu_l$ and $\Pi_\rho = \rho_g / \rho_l$ are the
 113 dynamic viscosity and density ratios, and the surface tension σ enters through the Weber
 114 number $\text{We} = \sigma \rho_l^{-1} \mathcal{U}_l^{-2} \mathcal{L}^{-1}$. The orthonormal surface coordinate system is constructed by
 115 $\mathbf{n} = [-\partial_x h, 1] (1 + \partial_x^2 h)^{-1/2}$ and $\boldsymbol{\tau} = [1, \partial_x h] (1 + \partial_x^2 h)^{-1/2}$, from which we obtain the film
 116 surface curvature $\kappa = -\nabla \cdot \mathbf{n}$.

117 We perform two types of calculations based on the first principles (2.1) to validate our
 118 low-dimensional model. First, we solve the OS linear stability problem (Tilley *et al.* 1994),
 119 assuming spatially growing normal modes (Barmak *et al.* 2016):

$$\begin{bmatrix} h \\ \Phi \\ \Psi \\ p_m \end{bmatrix} = \begin{bmatrix} h_0 \\ \Phi_0(y) \\ \Psi_0(y) \\ p_{m0}(x, y) \end{bmatrix} + \begin{bmatrix} \hat{h} \\ \phi(y) \\ \psi(y) \\ \hat{p}_m(y) \end{bmatrix} \exp \{i(kx - \omega t)\}, \quad (2.2)$$

121 where Φ and Ψ designate the stream functions in the liquid and gas, the subscript 0 denotes
 122 the flat-interface base flow, $k \in \mathbb{C}$ is the complex wave number of the perturbation, and
 123 $\omega \in \mathbb{R}$ its angular frequency. We focus on long-wave instability modes, which we track
 124 through numerical continuation using Auto07P (Lavalley *et al.* 2019), having checked with
 125 a Chebyshev collocation code (Barmak *et al.* 2016) that short wave modes remain stable
 126 throughout the studied parameter range. Second, we perform a DNS with the finite-volume
 127 solver Basilisk (Popinet 2015), based on the volume of fluid (VOF) and the continuum
 128 surface force (CSF) methods, following Dietze (2019). Here, we impose periodic conditions
 129 on a domain spanning the wavelength Λ .

130 Our low-dimensional model is based on the weighted residual integral boundary layer
 131 (WRIBL) approach (Ruyer-Quil & Manneville 1998; Kalliadasis *et al.* 2012), which de-
 132 scribes the flow via evolution equations for the flow rate q and film height h . We employ the
 133 two-phase formulation of Dietze & Ruyer-Quil (2013) written in Einstein notation ($m=l, g$
 135 and $n=l, g$):

$$\begin{aligned} \{S_m \partial_t q_m + F_{mn} q_m \partial_x q_n + G_{mn} q_j q_m \partial_x h\} &= -\text{We} \partial_{xxx} h \\ &+ \text{Fr}^{-2} (1 - \Pi_\rho) \{\sin(\phi) - \cos(\phi) \partial_x h\} + \text{Re}_m^{-1} C_m q_m \\ &+ \text{Re}_m^{-1} \{J_m q_m (\partial_x h)^2 + K_m \partial_x q_m \partial_x h + L_m q_m \partial_{xx} h + M_m \partial_{xx} q_m\}, \end{aligned} \quad (2.3a)$$

137

$$\partial_x q_l + \partial_t h = 0, \quad \partial_x q_g - X_g \partial_t h = 0, \quad (2.3b)$$

139 where q_l and q_g denote the liquid and gas flow rates (per unit width) and the coefficients
 140 $S_m, F_{mn}, G_{mn}, C_m, J_n, K_n, L_n,$ and M_n are known functions of the film height h
 141 (Dietze & Ruyer-Quil 2013).

142 We perform linear stability calculations by solving the dispersion equation $\text{DR}(\omega, k) = 0$,
 143 obtained by linearizing (2.3) around $[h_0, q_{l0}, q_{g0}]$, for $k = k_r + ik_i$ at a given $\omega \in \mathbb{R}$:

$$[h, q_l, q_g]^T = [h_0, q_{l0}, q_{g0}]^T + [\hat{h}, \hat{q}_l, \hat{q}_g]^T \exp \{i(kx - \omega t)\}, \quad (2.4a)$$

Cambridge University Press

Focus on Fluids articles must not exceed this page length

145

146

$$DR = i\omega^2 \{S_g - S_l\} + ik\omega \{F_{ml}q_m - F_{mg}q_m\} + ik^2 G_{mn}q_m q_n \quad (2.4b)$$

147

$$+ ik^2 Fr^{-2} \{\cos(\phi) - \Pi_\rho \cos(\phi)\} - i^3 k^4 We + \omega \{Re_g^{-1} C_g - Re_l^{-1} C_l\}$$

148

$$- k Re_m^{-1} \partial_h C_m q_m - i^2 k^3 Re_m^{-1} L_m q_m + i^2 k^2 \omega \{Re_g^{-1} M_g - Re_l^{-1} M_l\}.$$

150

We also compute nonlinear travelling-wave solutions (TWS), which remain unaltered in a reference frame moving at the wave speed c , through numerical continuation based on (2.3), using Auto07P (Doedel 2008). Our code allows to track TWS at the linearly most-amplified angular frequency $\omega = \omega_{\max}$, via the following constraints (Dietze *et al.* 2020):

154

$$DR(\omega_{\max}, k) = 0, \quad \partial_\omega k_i|_{\omega=\omega_{\max}} = 0. \quad (2.5)$$

155

Finally, we check the stability of nonlinear TWS via transient computations based on (2.3), using either periodic or inlet/outlet boundary conditions (Lavalle *et al.* 2020).

156

157 3. Results

158

We set the tilt angle to $\phi = 10^\circ$ and focus on a single fluid combination, a 83% by weight aqueous dimethylsulfoxide (DMSO) solution used in experiments (Dietze *et al.* 2009), where $\rho_l = 1098.3 \text{ kg/m}^3$, $\mu_l = 3.13 \text{ mPas}$, and $\sigma = 0.0484 \text{ N/m}$, in contact with ambient air. The Kapitza number for this combination is $Ka = \sigma \rho_l^{-1/3} g^{-1/3} \mu_l^{-4/3} = 509.5$. The channel height H^* is varied as $H^* = 1.2, 1.7, 1.8, 1.9, 2.1$, and 2.4 mm , which corresponds to values of $\eta = 2, 2.8, 3, 3.1, 3.4$, and 3.9 for the relative confinement:

164

$$\eta = H^* / h_0^*|_{M=1} = 1 / h_0|_{M=1}, \quad (3.1)$$

165

where $h_0|_{M=1}$ is the primary flow film thickness for an aerostatic gas pressure gradient, i.e. $M = \partial_x p_g / \sin(\phi) = 1$. We wish to confront the linear and nonlinear implications of increasing the counter-current gas flow rate at fixed Re_l . In particular, we wish to know whether nonlinear waves can be damped via increasing $|Re_g|$.

166

167

3.1. Most-amplified waves

169

Figure 2 demonstrates the effect of increasing the counter-current gas flow rate on the linearly most-amplified waves ($\omega = \omega_{\max}$) at fixed $Re_l = 15$ for different η values. Along each curve in panels 2a and 2c, the channel height H^* remains fixed while h_0 increases (between 10% for the strongest and 20% for the weakest confinement), and so η (3.1) specifies a representative confinement for each case, corresponding to the rightmost point of each curve (where $M = 1$). Curves in panel 2a track the maximum linear spatial growth rate $-k_i^{\max}$ in terms of Re_g , dashed lines corresponding to OS and solid lines to WRIBL calculations. At the largest η (filled squares, $\eta = 3.9$), the growth rate increases monotonically with $|Re_g|$, implying a gas-induced destabilization, up to the onset of absolute instability (AI), where $-k_{i\max}$ diverges (Vellingiri *et al.* 2015). Conversely, at very small η values (open squares and pentagons, $\eta = 2, 2.8$), the effect of the gas is monotonically stabilizing, up to the point of fully suppressing (S) the long-wave Kapitza instability (Lavalle *et al.* 2019; Kushnir *et al.* 2021). In the intermediate range (crosses, asterisks, and diamonds, $\eta = 3, 3.1$, and 3.4), the behaviour is non-monotonic, stabilization occurring at low and destabilization at large values of $|Re_g|$. Panels 2b ($\eta = 3.1$) and 2d ($\eta = 2$) represent dispersion curves for the non-monotonic and fully-stabilizing cases. Overall, there is quantitative agreement for $|Re_g| < 150$ between linear OS and WRIBL predictions in panels 2a, 2b, and 2d, whereas qualitative agreement is retained when approaching the AI limits.

185

186

187

6

G. Lavalle, S. Mergui, N. Grenier, and G. F. Dietze

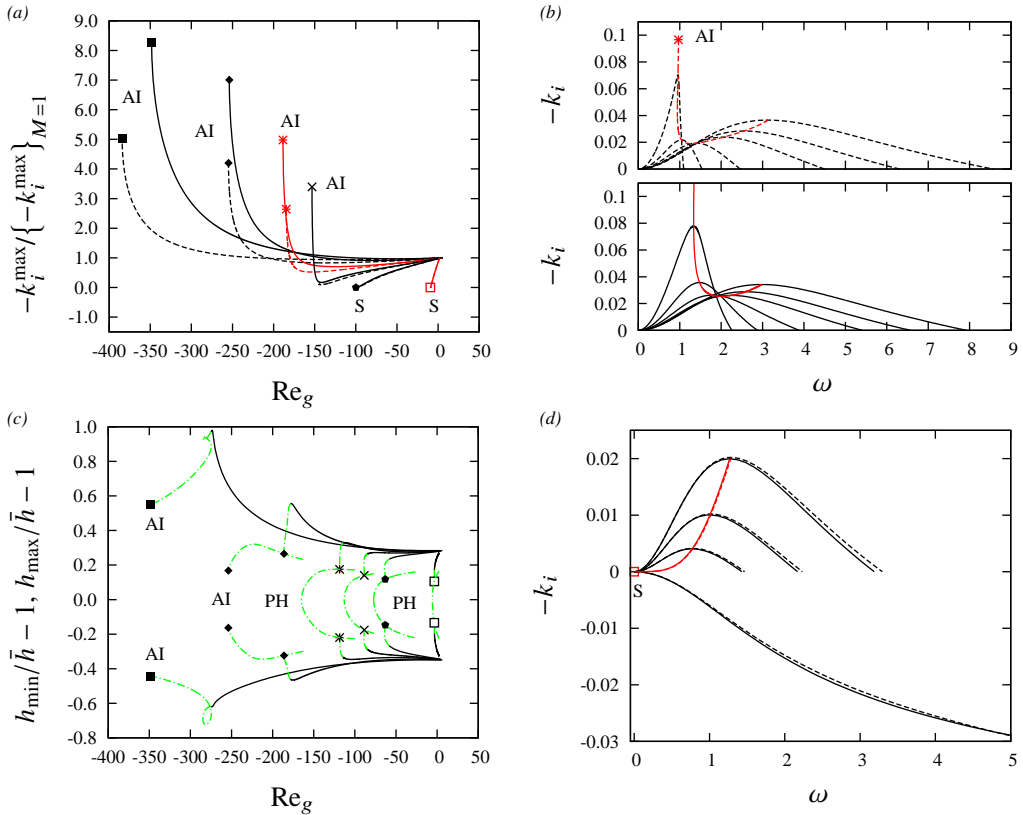


Figure 2: Most-amplified waves: $\phi=10^\circ$, $Re_l=15$, $Ka=509.5$. Linear (panels *a*, *b*, *d*) versus nonlinear (panel *c*) predictions. Filled squares: $\eta=3.9$, diamonds: $\eta=3.4$, asterisks: $\eta=3.1$, crosses: $\eta=3$; pentagons: $\eta=2.8$; open squares: $\eta=2$. (*a*) Maximal linear growth rate $-k_i^{\max} / \{-k_i^{\max}\}_{M=1}$, where $M=\partial_x p_g / \sin(\phi)$. Solid: WRIBL, dashed: OS; (*b*, *d*) dispersion curves $-k_i(\omega)$ for two cases from panel *a*. Red curves trace $-k_i^{\max}(\omega_{\max})$ up to absolute instability (AI) or full stabilization (S). (*b*) $\eta=3.1$; from right to left: $M=1$, $Re_g=-60$, -100 , -145 , -170 , and -184 ; (*d*) $\eta=2$; from right to left: $M=1$, $Re_g=4$, -7 , and -10 ; (*c*) amplitude of nonlinear TWS (WRIBL) at $\omega=\omega_{\max}$. PH denotes period-halving bifurcations and dot-dashed green lines identify periodically unstable TWS.

188 Panel 2c plots the upper and lower relative film height deflections $h_{\max}/\bar{h} - 1$
 189 for nonlinear TWS at $\omega=\omega_{\max}$, where $\bar{h}=\Lambda^{-1} \int_0^\Lambda h dx$ is the film height averaged over one
 190 wavelength, with $\bar{h} \neq h_0$ in the case of nonlinear waves. For $\eta=3, 3.1$, and 3.4 , TWS display a
 191 non-monotonic trend that is opposed to the linear one. That is, $h_{\max}/\bar{h} - 1$ in panel 2c, which
 192 we will refer to as the wave amplitude, first increases and then decreases with increasing
 193 $|Re_g|$, whereas $-k_i^{\max} / \{-k_i^{\max}\}_{M=1}$ in panel 2a first decreases and then increases. Conversely,
 194 for $\eta=2$ and 2.8 , the nonlinear and linear trends both imply stabilization, and, for $\eta=3.9$, they
 195 both imply destabilization, at least up to the amplitude maximum in panel 2c. Except for
 196 the two weakest confinements ($\eta=2, 2.8, 3, 3.1$), TWS are bounded by a nonlinear wave
 197 suppression, where $h_{\max}=h_{\min}$, resulting from period-halving (PH) bifurcations (marked by
 198 symbols), which sets in before the linear AI and S thresholds in panel 2a. Panel 3a shows
 199 wave profiles leading up to such a PH bifurcation ($\eta=3$). The sole precursory capillary ripple
 200 is seen to grow until splitting the wave into two identical halves. Conversely, for $\eta=3.9$ (panel
 201 3b), the capillary ripple disappears when increasing $|Re_g|$ toward the AI limit.

202 We conclude from figure 2 that linear stability predictions can be misleading. In particular,

Superconfined falling liquid films

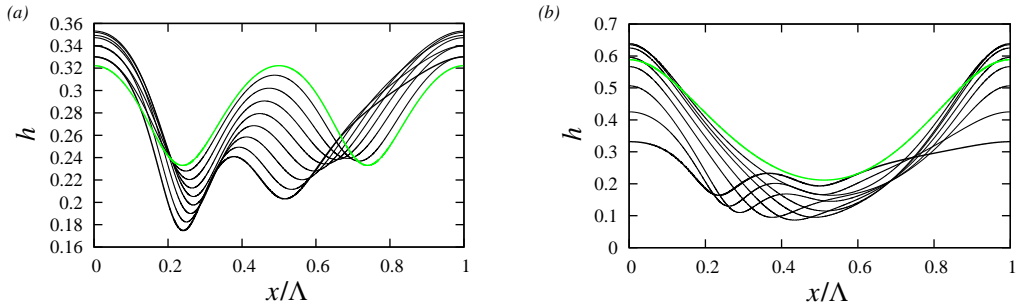


Figure 3: Wave profiles of TWS from panel 2c. (a) $\eta=3$ (cross in panel 2c). Approaching the PH bifurcation: $Re_g=-37$ (thick solid) to $Re_g=-88$ (green); (b) $\eta=3.9$ (filled square in panel 2c). Suppression of the capillary ripple while approaching the AI limit: $Re_g=-79$ (thick solid) to $Re_g=-348$ (green).

203 the amplitude of nonlinear waves may grow with increasing counter-current gas velocity,
 204 even though the linear growth rate decreases. Further, TWS become unstable to periodic
 205 secondary instability modes (dot-dashed lines in panel 2c) beyond a threshold Re_g , which
 206 we have determined via transient periodic computations started from TWS. These periodic
 207 modes do not lead to dangerous events, but TWS are also prone to a subharmonic instability
 208 in the case of a spatially-evolving film (Movie1.avi). Originally identified in unconfined
 209 films (Liu & Gollub 1993), this instability triggers wave coalescence events (Chang *et al.*
 210 1996a) that can lead to intermittent flooding in long channels (Dietze & Ruyer-Quil 2013).

211

3.2. Solitary waves

212 We focus now on low-frequency solitary waves at a fixed wavelength $\Lambda=4.5\tilde{\Lambda}_{\max}$, where
 213 $\tilde{\Lambda}_{\max}$ denotes the linearly most-amplified wavelength for a passive outer phase, all other
 214 parameters remaining as in figure 2. These waves lie on the ascending branch of the linear
 215 dispersion curves in panels 2b and 2d, and thus the linear effect of increasing the gas flow
 216 is monotonous, either destabilizing ($\eta=3, 3.1, 3.4, 3.9$) or stabilizing ($\eta=2, 2.8$). Panel 4a
 217 represents the nonlinear response of solitary TWS, evidencing a monotonous gas-induced
 218 attenuation of the wave amplitude for $\eta=2, 2.8, 3$, and 3.1 . For $\eta=3$ and 3.1 , this nonlinear
 219 effect is opposed to the linear amplification, and both effects are inverted w.r.t. the initial
 220 response of the most-amplified waves (panels 2a, 2c). Solution branches of solitary TWS in
 221 panel 4a are bounded either by the linear thresholds of absolute instability (AI, $\eta=3, 3.1$, and
 222 3.4) and full stabilisation (S, $\eta=2$ and 2.8) from panel 2a, or by a nonlinear limit point (LP,
 223 $\eta=3.9$) that occurs slightly before (about 2% in terms of Re_g) the AI bound.

224 For the strongest confinement, $\eta=2$ (open squares in panel 4a), linear and nonlinear effects
 225 are aligned and stabilizing. In that case, the gas shapes the wave hump into an elongated
 226 flat-top form (panel 4d). In panel 4e, we compare this solution (solid line) with TWS in the
 227 limits $\Pi_p=0$ (red dot-dot-dashed) and $\Pi_\mu=0$ (blue dashed), which respectively deactivate the
 228 gas pressure and the gas-side viscous stresses in (2.1e) and (2.1f). From this comparison, we
 229 can conclude that the gas pressure gradient and not the gaseous viscous stresses are the cause
 230 for wave flattening. The flat-top TWS (also shown in figure 1), which we have reproduced
 231 with a DNS at slightly greater $Re_l=15.7$ (open circles in panel 4e), is stable in periodic
 232 transient computations, and undergoes only weak modulations in a spatially-evolving film
 233 (Movie2.avi).

234 For the weakest confinement, $\eta=3.9$, solitary TWS are more susceptible to secondary
 235 instability modes. We discuss this based on the wave profiles in panel 4b, which correspond
 236 to the TWS marked by open circles in panel 4a. The TWS at $Re_g=-145$ (thick solid profile in

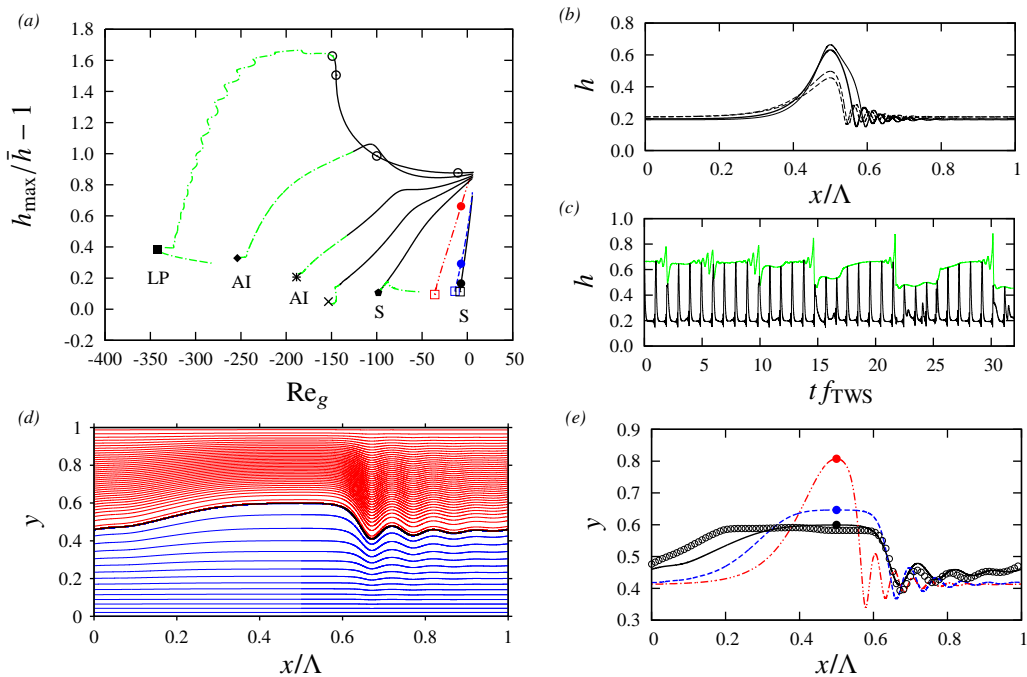


Figure 4: Solitary waves: $\phi=10^\circ$, $Re_l=15$, $Ka=509.5$, $\Lambda=4.5\tilde{\Lambda}_{\max}$. (a) Amplitude of nonlinear TWS (WRIBL). Right to left: $\eta=2$, 2 ($\Pi_\mu=0$), 2 ($\Pi_\rho=0$), 2.8, 3, 3.1, 3.4, and 3.9. Dot-dashed green lines highlight periodically unstable solutions; (b) wave profiles corresponding to open circles ($\eta=3.9$) in panel a. Bottom to top: $Re_g=-10$, -100, -145, and -149; (c) transient periodic computation started from thick-solid TWS in panel b. Black: local film height, green: wave height; (d) flat-top wave corresponding to black filled circle in panel 4a: $\eta=2$, $Re_g=-7$. Streamlines in the wave-fixed reference frame; (e) different limits of the $\eta=2$ solution in panel d (filled circles in panel a). Solid black: full inter-phase coupling; dashed blue: $\Pi_\mu=0$ in (2.1e) and (2.1f); dot-dot-dashed red: $\Pi_\rho=0$ in (2.1e); open circles: DNS at $M=\partial_x p_g/\sin(\phi)=M_{TWS}=84.8$, $Re_l=15.7$.

237 panel 4b, second from left open circle in panel 4a) still lies on the periodically-stable solution
 238 branch (solid curve in panel 4a). For this case, secondary instability can only arise through
 239 wave interactions. Pradas *et al.* (2013) showed, for the case of a passive atmosphere, that
 240 solitary waves can develop such interactions via the precursory capillary ripples, leading to
 241 oscillations around bound states, where neighbouring waves repeatedly approach and recoil
 242 from one another. Thereby, the approaching wave always grows, whereas the slowing wave
 243 always diminishes in amplitude. In the presence of a counter-current gas flow, we observe
 244 a secondary instability mode that involves a different wave interaction. We demonstrate
 245 this through an open-domain computation with coherent inlet forcing at the TWS frequency
 246 $f=\frac{2\pi}{\omega}=f_{TWS}=0.20$. Panels 5a and 5b (see also Movie3.avi) show that the instability produces
 247 solitary waves of diminishing amplitude that accelerate in the slipstream of their growing
 248 leading neighbours. This clearly differs from the behaviour of unconfined falling films, such
 249 as the above-mentioned oscillations around bound states (Pradas *et al.* 2013) or the well-
 250 known coarsening dynamics (Chang *et al.* 1996b), where larger-amplitude waves catch up
 251 with and accumulate the smaller ones travelling in front. The slipstreaming occurs in concert
 252 up- and downstream of a leading wave, and thus the latter is increasingly exposed to the
 253 counter-current gas flow, leading eventually to its destruction through a wave breaking event,
 254 before coalescence can occur.

255 When increasing the counter-current gas velocity further, TWS become periodically

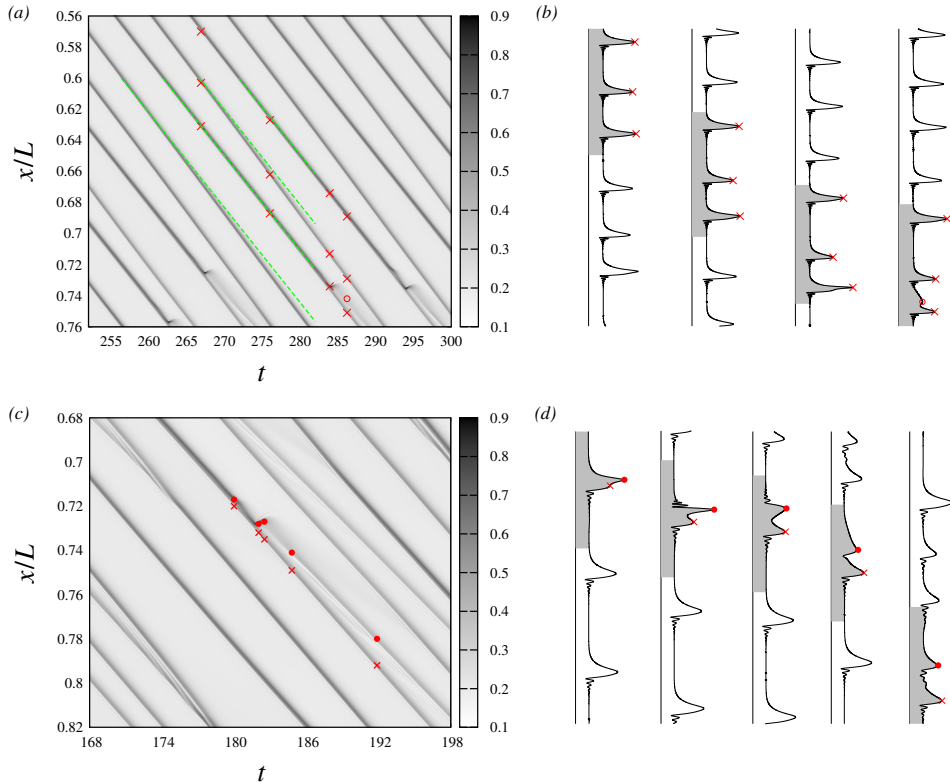


Figure 5: Slip streaming (panels *a, b*) and wave splitting (panels *c, d*) in solitary wave trains. Spatio-temporal computations with our WRIBL model (2.3) on an open domain of length $L=31.4 \Lambda_{TWS}$, applying coherent inlet forcing at $f=f_{TWS}$: $\phi=10^\circ$, $\eta=3.9$, $Re_l=15$, $Ka=509.5$. Space-time plots of the film height h (panels *a, c*), and wave profile snapshots (panels *b, d*). Parallel green dashed lines indicate initial TWS celerity. (*a, b*) $Re_g=-145$, $f_{TWS}=0.20$; (*c, d*) $Re_g=-149$, $f_{TWS}=0.19$. Red symbols identify primary/secondary wave maxima.

256 unstable (dot-dashed branches in panel 4a). For the TWS at $\eta=3.9$ and $Re_g=-149$ (thin
 257 solid profile in panel 4b, leftmost open circle in panel 4a), the instability leads to a self-
 258 sustained repeated breaking and reconstructing of the wave crest, as shown in panel 4c via
 259 a transient computation with periodicity conditions started from the TWS. In a spatially
 260 evolving film, which we have mimicked through an open-domain computation with inlet
 261 forcing frequency $f=f_{TWS}=0.19$ (panels 5c and 5d, and Movie4.avi), the instability leads
 262 to ubiquitous wave splitting events that refine the solitary wave train into a train of shorter and
 263 smaller daughter waves. This gas-induced *refining dynamics* can be viewed as the opposite
 264 of the coarsening dynamics observed in unconfined films (Chang *et al.* 1996b). We point out
 265 that isolated wave splitting events have been observed in noise-driven wave regimes, both
 266 experimentally (Kofman *et al.* 2017) and numerically (Dietze & Ruyer-Quil 2013).

267 4. Conclusion

268 In this work, we have demonstrated that linear stability predictions of strongly-confined
 269 falling liquid films can mislead in estimating the effect of a counter-current gas flow on
 270 the film's waviness. Both for waves of the most amplified frequency and for low-frequency
 271 solitary waves, we have identified situations where the linear and nonlinear responses are

272 opposed, i.e. linear waves are damped while nonlinear ones are amplified, or vice-versa. In
273 some cases, linear waves are bounded by absolute instability, whereas nonlinear waves are
274 fully suppressed via a period-halving bifurcation. Nonetheless, at very strong confinement,
275 both the linear and nonlinear responses imply stabilization and travelling-wave solutions
276 (TWS) resist secondary instability. This suggests that the risk of wave-induced flooding can
277 be lowered by strongly confining the flow. At weaker confinement, we have found two new
278 secondary instability modes not observed in unconfined films. The first tends to coarsen
279 the wave train, via smaller waves accelerating in the slipstream of their leading neighbours.
280 The second causes wave splitting events that refine the wave train into a sequence of less
281 dangerous shorter and smaller daughter waves.

282 Our two-dimensional analysis cannot account for the spanwise destabilization of TWS,
283 which entails the formation of three-dimensional waves in the downstream portion of
284 a spatially-evolving falling liquid film (Chang 1994; Liu *et al.* 1995; Scheid *et al.* 2006;
285 Kofman *et al.* 2014; Dietze *et al.* 2014; Kharlamov *et al.* 2015). Nonetheless, we expect our
286 conclusion on the stabilizing effect of strong confinement to extend to that situation. Firstly,
287 the inertia-driven three-dimensional secondary instability mode (Kofman *et al.* 2014) is
288 known to weaken at the small tilt angles considered here. In experiments, this translates
289 to quasi-two-dimensional wave fronts with only weak spanwise modulations, which are
290 maintained up to large gas velocities (Kofman *et al.* 2017). Secondly, the spanwise instability
291 mode is dictated by the wall-normal acceleration of liquid within the initially two-dimensional
292 wave hump. Thus, the gas-effect on the amplitude of two- and three-dimensional wave
293 humps is expected to be concurrent. This is supported by the weakly-confined experiments
294 of Kofman *et al.* (2017), where the counter-current gas flow amplified both instability modes.
295 In our strongly-confined setting, we expect the opposite, i.e. a damping of both modes.

296 The channel heights considered here ($1.2 \text{ mm} \leq H^* \leq 2.4 \text{ mm}$) lie in between the range
297 of classical (Vlachos *et al.* 2001) falling-film experiments ($H^* \geq 5 \text{ mm}$) and micro-channel
298 (Zhang *et al.* 2009; Hu & Cubaud 2018) falling-film experiments ($H^* \leq 1 \text{ mm}$). Also,
299 strongly-confined experiments have generally not considered small tilt angles. Our numerical
300 computations suggest that this uncharted part of the regime map deserves experimental
301 attention. Should experiments confirm our findings, it would mean that surface waves
302 can be maintained in very compact liquid/gas exchangers without the risk of flooding.
303 Current microreactor designs consist of arrays of narrow grooves, where the film surface is
304 pinned laterally (Al-Rawashdeh *et al.* 2008), and this effectively suppresses surface waves
305 (Pollak *et al.* 2011), solving the flooding problem, but at the cost of waiving the substantial
306 wave-induced intensification of heat/mass transfer (Yoshimura *et al.* 1996). Our results
307 suggest relaxing the lateral confinement in such devices to allow for the development of
308 surface waves. Experiments in horizontal wavy liquid-film/gas flows through mini-gaps
309 (Kabov *et al.* 2007, 2011) have shown that it is possible to produce the strong crosswise
310 confinement levels studied here ($H^*=2 \text{ mm}$) at weak spanwise confinement ($W^*=40 \text{ mm}$).

311 Acknowledgements

312 We appreciate helpful discussions with J. P. Hulin. This work was supported by the ANR
313 wavyFILM project, grant ANR-15-CE06-0016-01 of the French Agence Nationale de la
314 Recherche.

315 Declaration of interests

316 The authors report no conflict of interest.

317 **Supplementary data**

318 The manuscript includes four supplementary movies.

REFERENCES

- 319 AL-RAWASHDEH, M., HESSEL, V., LÖB, P., MEVISSSEN, K. & SCHÖNFELD, F. 2008 Pseudo 3-d simulation of a
320 falling film microreactor based on realistic channel and film profiles. *Chem. Eng. Sci.* **63**, 5149–5159.
- 321 ALEKSEENKO, S. V., AKTERSHEV, S. P., CHERDANTSEV, A. V., KHARLAMOV, S. M. & MARKOVICH, D. M. 2009
322 Primary instabilities of liquid film flow sheared by turbulent gas stream. *Int. J. Multiphase Flow* **35**,
323 617–627.
- 324 BARMAN, I., GELFGAT, A., VITOSHKIN, H., ULLMAN, A. & BRAUNER, N. 2016 Stability of stratified two-phase
325 flows in horizontal channels. *Phys. Fluids* **28**, 044101.
- 326 CHANG, H. C. 1994 Wave evolution on a falling film. *Annu. Rev. Fluid Mech.* **26**, 103–136.
- 327 CHANG, H. C., DEMEKHIN, E. A. & KALADIN, E. 1996a Simulation of noise-driven wave dynamics on a
328 falling film. *AIChE J.* **42** (6), 1553–1568.
- 329 CHANG, H. C., DEMEKHIN, E. A., KALADIN, E. & YE, Y. 1996b Coarsening dynamics of falling-film solitary
330 waves. *Phys. Rev. E* **54** (2), 1467–1477.
- 331 DIETZE, G. F. 2019 Effect of wall corrugations on scalar transfer to a wavy falling liquid film. *J. Fluid Mech.*
332 **859**, 1098–1128.
- 333 DIETZE, G. F., AL-SIBAI, F. & KNEER, R. 2009 Experimental study of flow separation in laminar falling
334 liquid films. *J. Fluid Mech.* **637**, 73–104.
- 335 DIETZE, G. F., LAVALLE, G. & RUYER-QUIL, C. 2020 Falling liquid films in narrow tubes: occlusion scenarios.
336 *J. Fluid Mech.* **894**, A17.
- 337 DIETZE, G. F., ROHLFS, W., NÄHRICH, K., KNEER, R. & SCHEID, B. 2014 Three-dimensional flow structures
338 in laminar falling liquid films. *Journal of Fluid Mechanics* **743**, 75–123.
- 339 DIETZE, G. F. & RUYER-QUIL, C. 2013 Wavy liquid films in interaction with a confined laminar gas flow. *J.*
340 *Fluid Mech.* **722**, 348–393.
- 341 DOEDEL, E. J. 2008 AUTO07P: Continuation and bifurcation software for ordinary differential equations.
342 *Montreal Concordia University*.
- 343 DROSOS, E. I. P., PARAS, S. V. & KARABELAS, A. J. 2006 Counter-current gas-liquid flow in a vertical narrow
344 channel - liquid film characteristics and flooding phenomena. *Int. J. Multiphase Flow* **32**, 51–81.
- 345 HU, X. & CUBAUD, T. 2018 Viscous wave breaking and ligament formation in microfluidic systems. *Physical*
346 *Review Letters* **121**, 044502.
- 347 KABOV, O. A., LYULIN, YU. V., MARCHUK, I. V. & ZAITSEV, D.V. 2007 Locally heated shear-driven liquid
348 films in microchannels and minichannels. *Int. J. Heat Fluid Flow* **28**, 103–112.
- 349 KABOV, O. A., ZAITSEV, D.V., V.V., CHEVERDA & BAR-COHN, A. 2011 Evaporation and flow dynamics of
350 thin, shear-driven liquid films in microgap channels. *Exp. Therm Fluid Sci.* **35**, 825–831.
- 351 KALLIADASIS, S., RUYER-QUIL, C., SCHEID, B. & VELARDE, M. G. 2012 *Falling Liquid Films, Applied*
352 *Mathematical Sciences*, vol. 176. Springer Verlag.
- 353 KAPITZA, P. L. 1948 Wave flow of thin layer of viscous fluid (in Russian). *Zhurn. Eksper. Teor. Fiz.* **18** (1),
354 3–28.
- 355 KHARLAMOV, S. M., GUZANOV, V. V., BOBYLEV, A. V., ALEKSEENKO, S. V. & MARKOVICH, D. M. 2015 The
356 transition from two-dimensional to three-dimensional waves in falling liquid films: Wave patterns
357 and transverse redistribution of local flow rates. *Physics of Fluids* **27**, 114106.
- 358 KOFMAN, N., MERGUI, S. & RUYER-QUI, C. 2014 Three-dimensional instabilities of quasi-solitary waves in
359 a falling liquid film. *Journal of Fluid Mechanics* **757**, 854–887.
- 360 KOFMAN, N., MERGUI, S. & RUYER-QUIL, C. 2017 Characteristics of solitary waves on a falling liquid film
361 sheared by a turbulent counter-current gas flow. *Int. J. Multiphase Flow* **95**, 22–34.
- 362 KUSHNIR, R., BARMAN, I., ULLMANN, A. & BRAUNER, N. 2021 Stability of gravity-driven thin-film flow in
363 the presence of an adjacent gas phase. *International Journal of Multiphase Flow* **135**, 103443.
- 364 LAVALLE, G., GRENIER, N., MERGUI, S. & DIETZE, G. F. 2020 Solitary waves on superconfined falling liquid
365 films. *Physical Review Fluids* **5** (3), 032001(R).
- 366 LAVALLE, G., LI, Y., MERGUI, S., GRENIER, N. & DIETZE, G. F. 2019 Suppression of the kapitza instability
367 in confined falling liquid films. *J. Fluid Mech.* **860**, 608–639.
- 368 LIU, J. & GOLLUB, J. P. 1993 Onset of spatially chaotic waves on flowing films. *Phys. Rev. Lett.* **70** (15),
369 2289–2292.

- 370 LIU, J., SCHNEIDER, J.B. & GOLLUB, J. P. 1995 Three-dimensional instabilities of film flows. *Physics of*
371 *Fluids* **7** (1), 55–67.
- 372 POLLAK, T., HAAS, A. & AKSEL, N. 2011 Side wall effects on the instability of thin gravity-driven films -
373 from long-wave to short-wave instability. *Physics of Fluids* **23**, 094110.
- 374 POPINET, S. 2015 A quadtree-adaptive multigrid solver for the serre-green-naghdhi equations. *J. Comput.*
375 *Phys.* **302**, 336–358.
- 376 PRADAS, M., KALLIADASIS, S., NGUYEN, P.-K. & BONTOZOGLU, V. 2013 Bound-state formation in interfacial
377 turbulence: direct numerical simulations and theory. *Journal of Fluid Mechanics* **716**, R2.
- 378 RUYER-QUIL, C. & MANNEVILLE, P. 1998 Modeling film flows down inclined planes. *Eur. Phys. J. B* **6** (2),
379 277–292.
- 380 SAMANTA, A. 2014 Shear-imposed falling film. *J. Fluid Mech.* **753**, 131–149.
- 381 SCHEID, B., RUYER-QUIL, C. & MANNEVILLE, P. 2006 Wave patterns in film flows: modelling and three-
382 dimensional waves. *J. Fluid Mech.* **562**, 183–222.
- 383 SCHMIDT, P., NÁRAIGH, L. Ó., LUCQUIAUD, M. & VALLURI, P. 2016 Linear and nonlinear instability in vertical
384 counter-current laminar gas-liquid flows. *Phys. Fluids* **28**, 042102.
- 385 SUDO, Y. 1996 Mechanism and effects of predominant parameters regarding limitation of falling water in
386 vertical countercurrent two-phase flow. *J. Heat Transfer* **118** (3), 715–724.
- 387 TILLEY, B. S., DAVIS, S. H. & BANKOFF, S. G. 1994 Linear stability theory of two-layer fluid flow in an
388 inclined channel. *Phys. Fluids* **6** (12), 3906–3922.
- 389 TRIFONOV, Y. Y. 2010a Counter-current gas-liquid wavy film flow between the vertical plates analyzed using
390 the Navier-Stokes equations. *AIChE J.* **56** (8), 1975–1987.
- 391 TRIFONOV, Y. Y. 2010b Flooding in two-phase counter-current flows: Numerical investigation of the gas-
392 liquid wavy interface using the Navier-Stokes equations. *Int. J. Multiphase Flow* **36**, 549–557.
- 393 TRIFONOV, Y. Y. 2017 Instabilities of a gas-liquid flow between two inclined plates analyzed using the
394 Navier-Stokes equations. *Int. J. Multiphase Flow* **95**, 144–154.
- 395 TRIFONOV, Y. Y. 2020 Linear and nonlinear instabilities of a co-current gas-liquid flow between two inclined
396 plates analyzed using the Navier-Stokes equations. *Int. J. Multiphase Flow* **122**, 103159.
- 397 TSELUIKO, D. & KALLIADASIS, S. 2011 Nonlinear waves in counter-current gas-liquid film flow. *J. Fluid*
398 *Mech.* **673**, 19–59.
- 399 VALLURI, P., MATAR, O. K., HEWITT, G. F. & MENDES, M. A. 2005 Thin film flow over structured packings
400 at moderate Reynolds numbers. *Chem. Eng. Sci.* **60**, 1965–1975.
- 401 VELLINGIRI, R., TSELUIKO, D. & KALLIADASIS, S. 2015 Absolute and convective instabilities in counter-
402 current gas-liquid film flows. *J. Fluid Mech.* **763**, 166–201.
- 403 VLACHOS, N. A., PARAS, S. V., MOUZA, A. A. & KARABELAS, A. J. 2001 Visual observations of flooding in
404 narrow rectangular channels. *Int. J. Multiphase Flow* **27**, 1415–1430.
- 405 YOSHIMURA, P. N., NOSOKO, P. & NAGATA, T. 1996 Enhancement of mass transfer into a falling laminar
406 liquid film by two-dimensional surface waves-some experimental observations and modeling. *Chem.*
407 *Eng. Sci.* **51** (8), 1231–1240.
- 408 ZHANG, H., CHEN, G., YUE, J. & YUAN, Q. 2009 Hydrodynamics and mass transfer of gas-liquid flow in a
409 falling film microreactor. *AIChE J.* **55** (5), 1110–1120.